

# Geophysical Research Letters<sup>®</sup>

## RESEARCH LETTER

10.1029/2021GL096037

### Key Points:

- Probability distributions of precipitation clusters (contiguous precipitating regions) are reasonably reproduced in CMIP6 models
- Under global warming, models project increases in frequencies of both clusters with large size and clusters with large precipitation
- These increases primarily occur over tropical regions with a large incidence of heavily precipitating systems in current climate

### Supporting Information:

Supporting Information may be found in the online version of this article.

### Correspondence to:

F. Ahmed,  
fiaz@ucla.edu

### Citation:

Dulguerov, L., Ahmed, F., & Neelin, J. D. (2022). Extreme tropical precipitation clusters show strong increases in frequency under global warming in CMIP6 models. *Geophysical Research Letters*, 49, e2021GL096037. <https://doi.org/10.1029/2021GL096037>

Received 3 SEP 2021  
Accepted 9 DEC 2021

## Extreme Tropical Precipitation Clusters Show Strong Increases in Frequency Under Global Warming in CMIP6 Models

Leilani Dulguerov<sup>1</sup> , Fiaz Ahmed<sup>1</sup> , and J. David Neelin<sup>1</sup> 

<sup>1</sup>Department of Atmospheric and Oceanic Sciences, University of California, Los Angeles, CA, USA

**Abstract** Precipitation clusters are spatially contiguous precipitating regions. Large clusters in the tropics are rare, extreme events that include organized precipitating systems. Changes to the probability distributions of tropical precipitation clusters under global warming are examined using models from the coupled model intercomparison project Phase 6 (CMIP6). Every analyzed model projects significant increases in frequencies of both very large-sized clusters and clusters with very large area-integrated precipitation (cluster power). The occurrence probability for the highest historical cluster power values increases by a factor between 4 and 15 among models in the end-of-century SSP5-8.5 scenario. These changes primarily occur over the precipitating tropics: the western Pacific, Indian subcontinent, central and east Pacific convergence zones, and parts of South America. This spatial pattern is largely explained by Clausius-Clapeyron scaling of current climate cluster power values. Societal impacts of cluster power increases could be acute in coastal regions of the Indian subcontinent and western Pacific islands.

**Plain Language Summary** Spatially continuous precipitating points are called precipitation clusters. In the tropics, the largest of these clusters represent systems like hurricanes or groups of thunderstorms. Large clusters also release greater rainfall and therefore hold more potential for destruction. In this study, we use state of the art climate models to examine how precipitation clusters with very large size and rain amounts will change under global warming. All the models we analyzed agree that there will be significant increases in the frequency of large and heavily precipitating clusters. The models project between a 4 and 15 times increase in the frequency of clusters bearing the largest rain amounts. These increases are projected to happen predominantly over tropical regions with warm surface waters. We also found a simple hypothesis that explains these changes. This hypothesis is based on the fact that warmer air can hold more moisture. Increases in the frequency of precipitation clusters with large rain amounts could be particularly devastating for the islands of the western Pacific and heavily populated coastal regions of the Indian subcontinent.

## 1. Introduction

Tropical precipitation extremes are poised to intensify under global warming (O’Gorman, 2012; O’Gorman & Schneider, 2009; Romps, 2011). Pointwise precipitation statistics have been extensively examined (see reviews in Muller & Takayabu, 2020; O’Gorman, 2015). However, similar examinations of spatially contiguous precipitating points are less common. Observation-based studies (Hamada & Takayabu, 2018; Roca & Fiolleau, 2020; Tan et al., 2015) suggest that extreme tropical rainfall intensification is partly driven by increases in the frequency of spatially-extensive precipitating systems. It is imperative to quantify changes to these systems, given their significant socioeconomic risk (Doswell III et al., 1996; Peduzzi et al., 2012).

Precipitation clusters, defined as spatially contiguous precipitating regions, are useful entities when characterizing spatially-extensive precipitating systems. Two leading properties are naturally ascribed to precipitation clusters: (1) the cluster size (measured by cluster area  $a$ ) and (2) cluster-integrated precipitation, which can be expressed as latent heat release with units of power and is therefore termed cluster power,  $c$ . The observed probability density functions (pdfs) of cluster size and power display long power law ranges followed by a large-event cutoff (Peters et al., 2012; Quinn & Neelin, 2017a; Teo et al., 2017). The large-event cutoff values  $a_L$  and  $c_L$  respectively denote scales for cluster size and power that characterize the rapid probability drop in the medium-to-large events range of the pdfs. The cutoffs therefore act as measures of extreme events in terms of both size and rain amount. Events near and beyond the cutoffs are spatially-extensive precipitating systems that include large mesoscale convective systems and tropical cyclones (Peters et al., 2012; Quinn & Neelin, 2017a). A

stochastic prototype suggests that  $a_L$  and  $c_L$  are governed by moisture-convective feedbacks and nearest neighbor interactions (Ahmed & Neelin, 2019). Similar large-event cutoffs are also noted in pointwise precipitation statistics, including for rainfall accumulations (Martinez-Villalobos & Neelin, 2018; Neelin et al., 2017; Stechmann & Neelin, 2014) and daily-averaged rainfall (Martinez-Villalobos & Neelin, 2019).

Global climate models reasonably reproduce the cluster pdf shapes, and also indicate that the cluster power cutoff increases under global warming (Quinn & Neelin, 2017a, 2017b). However, many quantitative details of this increase are unknown; for instance: (a) how do the cluster power increases compare to Clausius-Clapeyron (CC) implied changes (Allen & Ingram, 2002; Kharin et al., 2013)?, (b) what is the spatial distribution of these increases?, and (c) how does  $a_L$  vary with warming, given the absence of a simple hypothesis for how precipitation cluster sizes should change. In this study we use models participating in Phase 6 of the coupled model inter-comparison project (CMIP6; Eyring et al., 2016) to probe the quantitative and spatial details of  $a_L$  and  $c_L$  changes under global warming. The cluster pdfs from CMIP6 models—in both current and future climates—alongside the observational baseline are discussed in Section 2. All models show  $a_L$  and  $c_L$  increases under global warming. These increases are quantified using risk ratios in Section 3. In Section 4, the spatial distribution of clusters with large power values is examined. Regions that would likely see the largest increases in the strength and frequency of the most heavily precipitating systems are highlighted.

## 2. Precipitation Cluster Probability Distributions

The observational baseline for the cluster statistics is established using TRMM 3B42 precipitation data (Huffman et al., 2007) on a  $0.25^\circ \times 0.25^\circ$  spatial grid with 3-hourly temporal frequency. The analysis domain covers the tropical region (30°N–30°S) for a 10-year time period (2005–2014). 10 CMIP6 models are analyzed. Three-hourly model precipitation fields from both historical and end-of-century shared socioeconomic pathway 5–8.5 (SSP5-8.5; O'Neill et al., 2016) runs are used. Ten-year time periods from both historical (2005–2014) and SSP5-8.5 runs (2091–2100) are used for all but one model (due to data availability; see Table S1 in Supporting Information S1). Spatially contiguous grid-points precipitating above 1 mm/hr are grouped to form precipitation clusters, using both observed and model precipitation fields. Sensitivity to the threshold precipitation used to create the clusters is tested (Texts S3 and S4). Models exhibit greater sensitivity than observations at low thresholds, but the primary results are unaffected for precipitation thresholds exceeding 0.75 mm/hr (Text S4 in Supporting Information S1). Using a precipitation threshold also eliminates spurious effects of the drizzle problem on the model cluster pdfs (Texts S2 and S3 in Supporting Information S1).

The cluster size and power pdfs for TRMM 3B42 and CMIP6 models are shown in Figure 1. As documented previously (Quinn & Neelin, 2017a; Teo et al., 2017), the TRMM precipitation cluster distributions display a long power range (over nearly 4 decades), followed by a large-event cutoff. The cluster size is expressed in units of  $\text{km}^2$ . Cluster power is expressed in units of GigaWatts (GW). The pdf of cluster power,  $p(c)$  is approximately described by:

$$p(c) \sim c^{-\tau} \exp\left(-\frac{c}{c_L}\right) \quad (1)$$

with a similar expression for cluster area. In Equation 1,  $\tau$  is the slope of the power-law range. From Equation 1, it is seen that the power law describes the distribution for small- and medium-sized events ( $c \ll c_L$ ), while the exponential describes the distribution for large events ( $c \sim c_L$ ). Figure 1 shows that the CMIP6 models qualitatively reproduce the shape of the observed cluster pdfs, including the power law range and a large-event cutoff (except for BCC-CSM2-MR; see Text S1). Most models have  $\tau$  values close to the observational baseline, although a few models exhibit larger departures (Text S1 in Supporting Information S1). Inter-model differences in the length of the power law range are also noted in Figure 1. These arise from horizontal resolution differences among models (Table S1 in Supporting Information S1), which limit the smallest sampled cluster size and power values.

The log-log plots (Figures 1a and 1b) show that for a given model, the power law range for the SSP5-8.5 clusters extends out to slightly larger values than for the historical clusters. This implies changes in  $a_L$  and  $c_L$  values under global warming. To more closely examine these changes, the cluster pdfs are presented on a log-linear plot in Figures 1c and 1d, which enlarges the pdf tails. A linear regression over the pdf tails yields the straight line fits in Figures 1c and 1d. The range for the linear fit begins at  $10^6 \text{ km}^2$  for  $a_L$  estimation, and at  $1.5 \times 10^6 \text{ GW}$  for  $c_L$  estimation. These values are chosen to ensure that the cutoff estimators are unaffected by the power law range; small

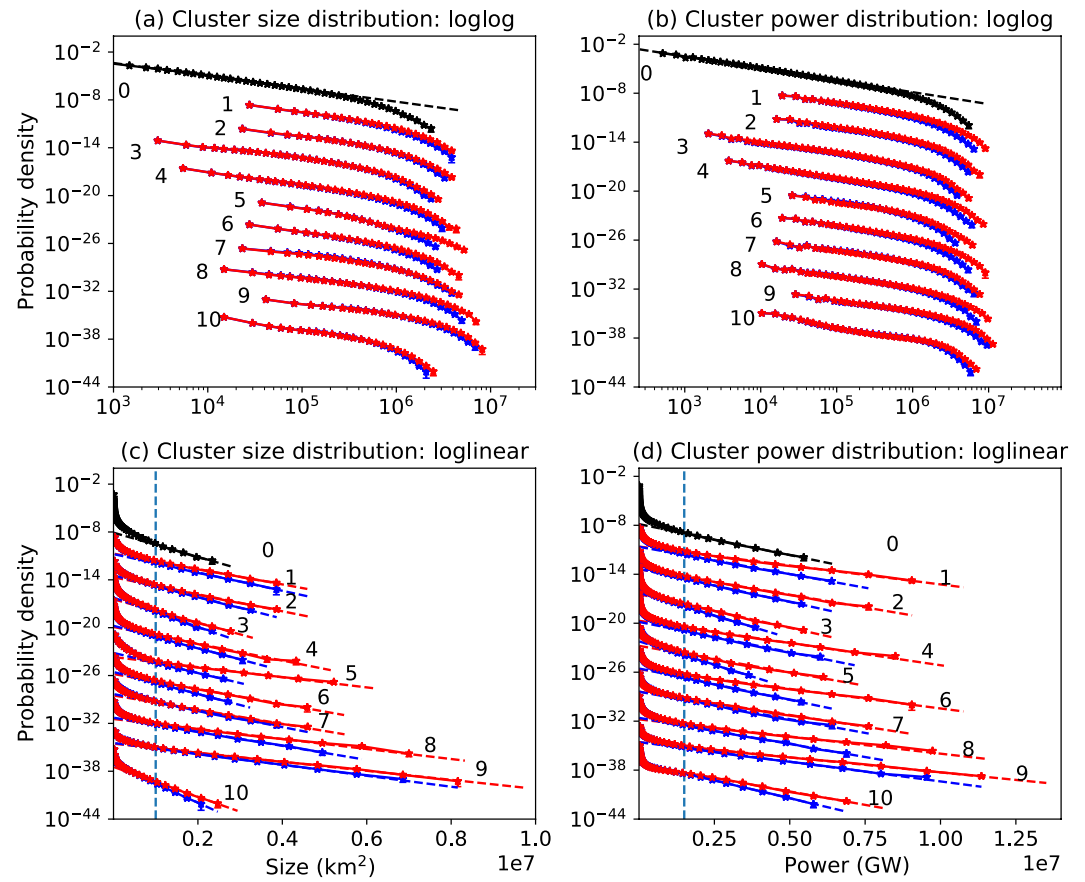


**Figure 1.** Precipitation cluster size and power pdfs from TRMM 3B42 (black) and CMIP6 models (historical in blue and SSP5-8.5 in red). The pdfs are spaced 2 decades apart on the log-y axis for clarity and are displayed using logarithmic (top row) and linear x-axes (bottom row). Reference power law slopes with values  $-1.6$  (panel a) and  $-1.5$  (panel b) are denoted by black dashed lines. The blue and red dashed lines in (c) and (d) denote linear fits used to estimate  $a_L$  and  $c_L$  (see text; Section 2); the linear fit range begins at values denoted by the dashed vertical lines in (c) and (d). The integers in each panel denote different CMIP6 models: 1-ACCESS-CM2; 2-CNRM-CM6-1; 3-CNRM-CM6-1-HR; 4-HadGEM3-GC31-MM; 5-IPSL-CM6A-LR; 6-KACE-1-0-G; 7-MIROC6; 8-MRI-ESM2-0; 9-NESM3; 10-BCC-CSM2-MR.

changes to these values do not qualitatively impact the results (Text S5 in Supporting Information S1). The goodness-of-fit for the straight lines in Figures 1c and 1d validates the use of the exponential in Equation 1 to capture the pdf tails—since exponentials appear as straight lines on log-linear axes. The slopes of the straight line fit ( $\approx -1/a_L$  in Figure 1c and  $\approx -1/c_L$  in Figure 1d) yield estimates for  $a_L$  and  $c_L$ . When estimated this way, considerable inter-model spread exists in the  $a_L$  and  $c_L$  values from CMIP6 models. Only a handful of model historical simulations quantitatively approach the observed  $a_L$  and  $c_L$  values (see Text S2). This is also inferred from Figures 1c and 1d by noting differences in the slopes of the log-linear fit between the observations (black) and the different historical runs (blue). These differences in cutoffs could arise from model differences in the details of moist physics (e.g., in the convective schemes), since the large-event cutoff is sensitive to the strength of moist-convective feedbacks (Ahmed & Neelin, 2019). Despite the spread in  $a_L$  and  $c_L$  values, the straight line slopes in Figures 1c and 1d are consistently shallower for the SSP5-8.5 runs than for the corresponding historical runs. This suggests that for every model examined, both the cluster size and power cutoffs are larger in the SSP5-8.5 run.

In addition to straight line fits in log-linear plots, the large-event cutoffs can also be estimated using the moment ratio. The cluster power moment ratio,  $c_M$  is given by:

$$c_M = \frac{\langle c^2 \rangle}{\langle c \rangle^2} . \quad (2)$$

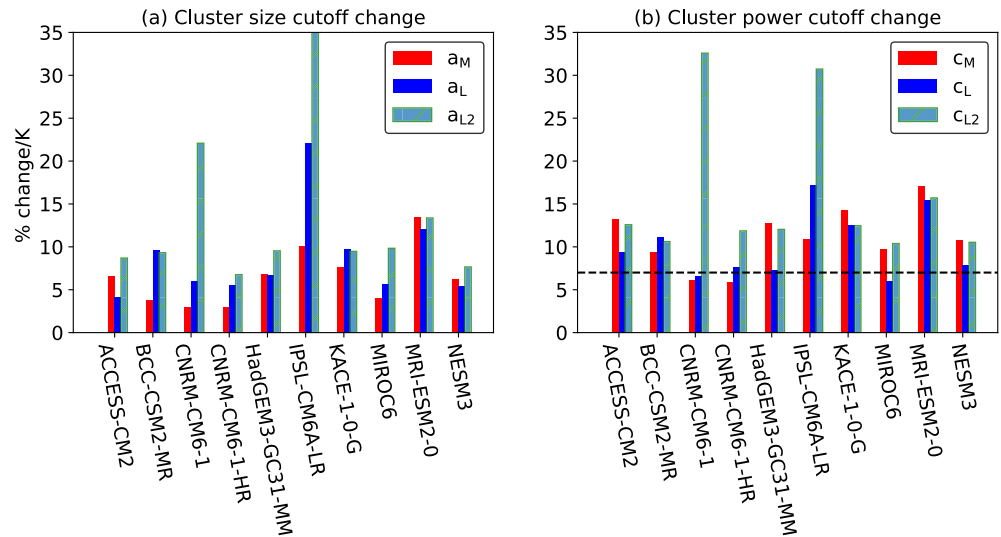


**Figure 2.** Differences in large-event cutoffs between historical and SSP5-8.5 model runs for (a) cluster area and (b) cluster power. The differences are expressed in units of percent change per K. The dashed black line in (b) marks the Clausius-Clapeyron implied change of 7%/K under CC-Case 1. Here,  $a_{L2}$  and  $c_{L2}$  denote changes predicted under CC-Case 2 (see text; Section 2).

Here  $\langle c \rangle$  and  $\langle c^2 \rangle$  are the first and second moments of cluster power respectively. The estimator in Equation 2 is proportional—but not equal—to  $c_L$  (Peters et al., 2010). Unlike  $c_L$ , which is estimated from the pdf tail,  $c_M$  depends on the full pdf range. Departures in the pdf shape away from Equation 1 can thus introduce additional sensitivities in the  $c_M$  computation. Nevertheless,  $c_M$  proves a useful second estimator for the large-event cluster power cutoff, and supplements the insights derived using  $c_L$  alone. A similar expression as in Equation 2 follows for the cluster size moment ratio  $a_M$ .

The quantitative details of how the large-event cutoff changes under warming are displayed in Figure 2. In this figure,  $a_L$  and  $c_L$  are the large-event cluster size and power cutoffs respectively estimated using straight line fits to the pdf tails (as discussed for Figures 1c and 1d). The  $a_M$  and  $c_M$  values are computed using the moment ratio estimator in Equation 2 for cluster size and power respectively. The differences in cutoffs between SSP5-8.5 and historical runs are normalized by the tropics-mean (30°N–30°S) surface temperature change for each model. This allows expression in units of %/K. Figures 2a and 2b show that for all models, both the large area ( $a_M$  and  $a_L$ ) and power ( $c_M$  and  $c_L$ ) cutoffs increase. This suggests that under global warming, spatially-extensive precipitating systems are projected to increase under measures of both size and cumulative precipitation.

Physical interpretations are now offered to interpret the details of  $a_L$  and  $c_L$  increases in Figure 2. Two limiting cases based on the CC-scaling are proposed: CC-Case 1 and CC-Case 2. In CC-Case 1 the cluster-enclosed precipitation in the historical run is assumed to scale with water vapor at the CC-implied rate, with cluster sizes staying fixed. This predicts a CC-scaling of  $c_L$  under global warming and no change in  $a_L$ . From Figure 2b, the CC-Case 1 scaling (dashed line) reasonably estimates  $c_L$  changes in five models: CNRM-CM6-1, CNRM-CM6-1-HR, HadGEM3-GC31-MM, MIROC6, and NESM3 all show close-to-CC increases ( $7 \pm 1\%/K$ ).

In CC-Case 2, the intensity of *all precipitating points* from the historical run is assumed to increase at 7%/K. This increases the cluster area because more points now cross the 1 mm/hr threshold. The combination of larger cluster areas and CC-scaled precipitation rates generates cluster power increases exceeding 7%/K (super-CC scaling). The area and power cutoff changes implied by CC-Case 2 are denoted by  $a_{L2}$  and  $c_{L2}$ . From Figure 2b,  $c_{L2}$  is an accurate estimator for at least three models exhibiting super-CC changes: BCC-CSM2-MR, KACE-1-0-G and MRI-ESM2-0. For two models, CNRM-CM6-1 and IPSL-CM6A-LR, CC-Case 2 noticeably overestimates  $c_{L2}$ ; for the other five models it moderately overestimates. The  $a_L$  changes in Figure 2b are also reasonably well-explained by CC-Case 2 for five models: BCC-CSM2-MR, CNRM-CM6-1-HR, KACE-1-0-G, MRI-ESM2-0, and NESM3. For other models, CC-Case 2 over-predicts the area cutoff changes. The CC-scaling of precipitation thus qualitatively explains why cluster size cutoffs increase under warming. The quantitative changes are overestimated

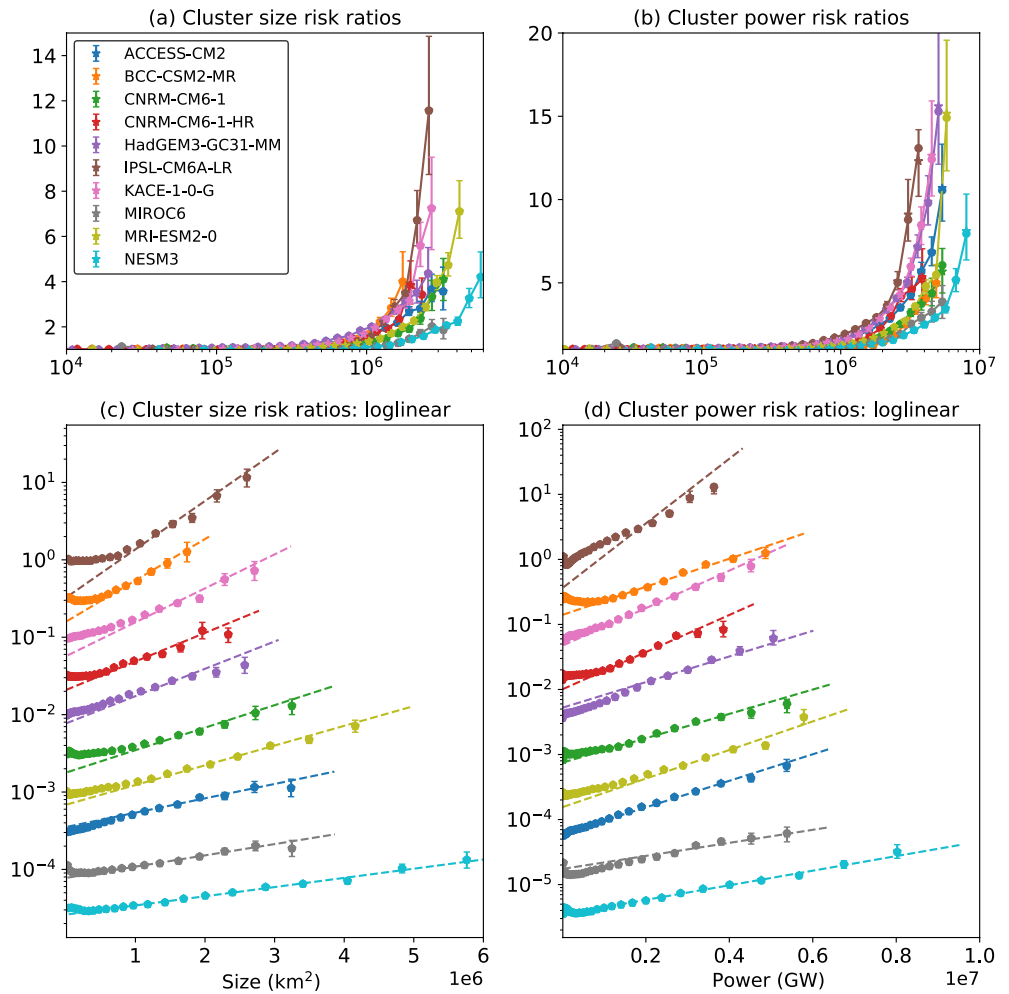


**Figure 3.** Cluster size (panels a and c) and power (panels b and d) risk ratios for different models. The risk ratios are displayed with linear (top row) and semi-log (bottom row) axes. The dashed lines in panels (c) and (d) are risk ratios estimated using  $a_L$  and  $c_L$  differences (see text; Section 3). The risk ratios in the bottom row are vertically spaced for clarity.

in half the models, plausibly because smaller rain rates near the cluster boundary scale slower than CC. The cluster size cutoff increases also impact the cluster power cutoff changes. Comparing Figures 2a and 2b, it is seen that modest  $a_L$  increments are associated with near-CC  $c_L$  increases, and large  $a_L$  increments with super-CC  $c_L$  increases.

### 3. Risk Ratios and Changes in the Large-Event Range

Risk ratios (RRs; Fischer & Knutti, 2015; Stott et al., 2004) are useful when summarizing the increased likelihood of events under different warming scenarios. Conditional RRs (Neelin et al., 2017; Quinn & Neelin, 2017a) further assess the increased likelihood for a given cluster size or power. These are computed as the ratio of the cluster pdf (size and power) in the SSP5-8.5 run to that in the historical run. Figure 3 shows the conditional RRs from each CMIP6 model, where the RR is conditioned on the value of cluster size (Figures 3a and 3c) and power (Figures 3b and 3d). For each model, an uncertainty measure for the conditional RR is generated from a bootstrapping procedure. The cluster pdfs for the historical and SSP5-8.5 scenarios are first reproduced 1,000 times by sampling the original distribution with replacement. The conditional RRs are then computed for each ensemble member. The 5th and 95th percentiles of this 1,000-member ensemble bound the error bars in Figure 3.

Figures 3a and 3b show that under global warming, the probability of encountering small-to-medium clusters (in terms of either size or power) is not greatly increased, since the conditional RR is  $\sim 1$ . However, the likelihood

of encountering very large events increases rapidly; the conditional RRs for cluster size and power appear to increase exponentially. Most models project at least a doubling in probability for the very largest cluster size that occurs with sufficient frequency to be captured in the historical sample (ranging between  $\sim 2$  and  $6 \times 10^6$  km<sup>2</sup> among models). The chance of encountering the most heavily raining clusters jumps by at least 4 times. Half the models (ACCESS-CM2, HadGEM3-GC31-MM, IPSL-CM6A-LR, KACE-1-0-G and MRI-ESM2-0) project a greater than 10 times increase in probability for the very largest values of cluster power (which varies between  $\sim 3$  and  $6 \times 10^6$  GW among these models). The uncertainty measure from the bootstrapping also increases with cluster size and power as a consequence of the increased rarity of events beyond the large-event cutoff.

The near-exponential increase in RR inferred from Figures 3a and 3b is a property of the cluster pdf shape from Equation 1. The form in Equation 1 suggests that the conditional RR for cluster power can be estimated by:

$$\text{conditional RR}(c) = \exp \left( c \left[ \frac{c_{L-SSP} - c_{L-HIST}}{c_{L-SSP} \times c_{L-HIST}} \right] \right), \quad (3)$$

where  $c_{L-SSP}$  and  $c_{L-HIST}$  are the large-event cluster power cutoffs for the SSP5-8.5 and historical simulations respectively. A similar expression follows for the cluster area conditional RR. Equation 3 holds provided that the power law slope  $\tau$  is unchanged between historical and SSP5-8.5 cluster pdfs, which is true for the models analyzed here (Text S1). This expression predicts an exponential increase in conditional RR when  $c_{L-SSP} > c_{L-HIST}$ . Using the linear fit estimates for  $a_L$  and  $c_L$  from Figures 1c and 1d, and the expression in Equation 3, an estimate for the conditional RR is computed. This estimate is overlaid on the directly computed conditional RRs in Figures 3c and 3d. These quantities are displayed on log-linear axes to present exponential changes as straight lines. It is seen that for most models, Equation 3 is a reasonably good estimator of the large-event conditional RR; although departures are also seen, most notably for IPSL-CM6A-LR. One reason for these departures could be deviations in the functional form of the pdfs from Equation 1. Overall, Figure 3 highlights that under global warming, the frequencies of precipitating systems with large size as well as those with large cumulative precipitation increase disproportionately when compared to small and medium events.

#### 4. Spatial Distribution of Large-Event Clusters

We now examine how the projected increase in the frequency of heavily precipitating systems manifests in space. First, the 99.9th percentile cluster power ( $c_{99.9}$ ) is estimated for both TRMM 3B42 and CMIP6 data. The  $c_{99.9}$  value for CMIP6 models is computed using each model's *historical run only*. Compared to CMIP6 models, TRMM 3B42 has a finer horizontal resolution, and consequently, a greater proportion of clusters with small power values (Figure 1b), which impacts the percentile computation. To minimize these impacts and to provide a more direct comparison to the models, cluster power percentiles are recalculated omitting values smaller than  $5 \times 10^3$  GW from the TRMM 3B42 analysis. This procedure quantitatively alters the TRMM 3B42  $c_{99.9}$  value but does not qualitatively impact the results. The computed  $c_{99.9}$  values are large in absolute terms: about  $(2.5 \pm 0.8) \times 10^6$  GW in the CMIP6 historical ensemble and  $1.8 \times 10^6$  GW in TRMM 3B42. Next, a cluster centroid or the precipitation weighted center-of-mass ( $\mathbf{x}_{COM}$ ) is computed for *each cluster* using:

$$\mathbf{x}_{COM} = \frac{\sum_i \mathbf{x}_i p_i}{\sum_i p_i}, \quad (4)$$

where  $\mathbf{x}_i$  denotes the latitude and longitude coordinates for each grid cell within a cluster, and  $p_i$  is the precipitation of that grid cell. The tropical region is then divided into coarse  $10^\circ$  latitude  $\times$   $20^\circ$  longitude grid boxes, and every cluster is assigned to one of these boxes based on its  $\mathbf{x}_{COM}$  value. The number of clusters in each grid box with power exceeding  $c_{99.9}$  is then computed and normalized by the time period of sampling in years. This yields a metric  $n_{99.9}$  for extreme precipitation clusters with units of cluster counts/year.

Figure 4a displays the spatial distribution of  $n_{99.9}$  for TRMM 3B42. It is seen that the clusters with large power are predominantly situated over the Indian and western Pacific Oceans, with the very largest counts over Southeast Asia. Interestingly, other climatologically precipitating zones such as the central and east Pacific convergence zones and the Congo Basin all show comparatively fewer precipitation clusters with large power. Figure 4b shows the multi-model mean of  $n_{99.9}$  from CMIP6 historical simulations. The observed spatial pattern of  $n_{99.9}$  is qualitatively reproduced by the CMIP6 multi-model mean. This skill is particularly noteworthy given the ab-

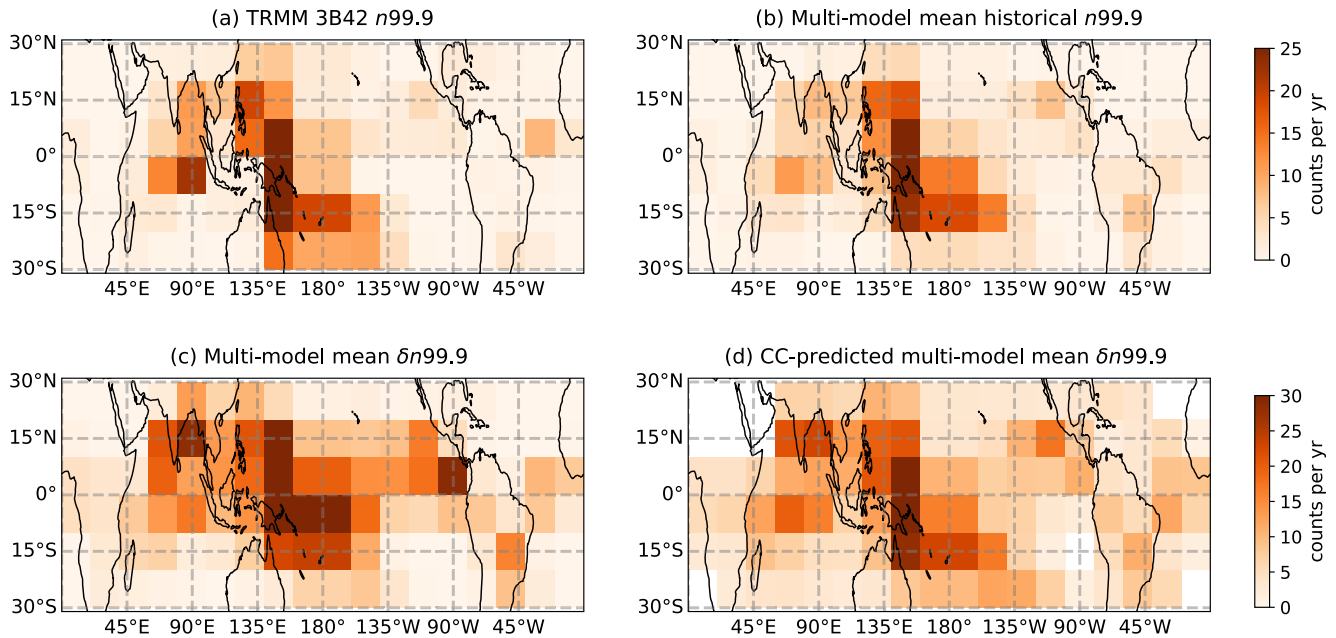


**Figure 4.** The (a) TRMM 3B42 and (b) CMIP6 multi-model mean values of  $n_{99.9}$  (units of counts/year of large clusters; see text, Section 4). (c) The multi-model mean and (d) CC-predicted changes in  $n_{99.9}$  between SSP5-8.5 and historical scenarios.

sence of high-resolution convective dynamics in CMIP6 models. This skill also increases confidence in the model ability to project future changes in the incidence of precipitation clusters with large power.

For each model, and for each coarsened grid box, the difference between the  $n_{99.9}$  values in the SSP5-8.5 and historical simulations (termed  $\delta n_{99.9}$ ) is computed. The result is a spatial pattern of change under global warming of the cluster counts with large power. The multi-model mean of  $\delta n_{99.9}$  is displayed in Figure 4c. This figure shows that CMIP6 models project significant increases in the number of clusters with large power over the Indian subcontinent and the western Pacific Ocean. This overlaps with regions already exhibiting the greatest incidence of clusters with large power in current climate (Figures 4a and 4b), exemplifying a form of the rich-get-richer phenomenon (Chou & Neelin, 2004; Tan et al., 2015; Trenberth, 2011). Other regional hot-spots for extreme cluster count increases include the central and eastern Pacific Inter-tropical convergence zone (ITCZ), and parts of South America. The projected changes over the Atlantic ITCZ and the Congo Basin appear more muted when compared to the other climatologically precipitating zones.

An explanatory model for the multi-model pattern of  $\delta n_{99.9}$  is constructed using the CC relationship. For each model, the tropics-mean surface temperature is used to scale the cluster power from historical simulations and provide an  $n_{99.9}$  prediction for the SSP5-8.5 runs. For a model with  $\delta T$  change in the tropics-mean surface temperature under warming, the cluster power for every historical model cluster is scaled by  $1 + \delta T \times 0.07$ —the same as CC-Case 1 in Section 2. The change in the number of clusters exceeding each model historical run's  $c_{99.9}$  value is then computed. The multi-model mean of this quantity is displayed in Figure 4d. It is seen that the broad regional pattern of cluster power increase—over the Indian subcontinent, the western Pacific and part of South America—as well as the lack of strong enhancement over the Atlantic ITCZ and the Congo Basin from Figure 4c is present in the CC approximation (Figure 4d). Some regional changes in  $\delta n_{99.9}$  are not captured by the CC-prediction, such as the increases over the central and eastern Pacific ITCZ. Nevertheless, the CC-prediction offers a leading order explanation for the pattern of global warming induced changes in precipitating systems with large cluster power.

## 5. Discussion and Conclusions

Statistics of tropical precipitation clusters (contiguous precipitating regions) are examined using TRMM observations and CMIP6 models. The probability distributions of cluster size and power (cumulative precipitation) from most model historical simulations agree with TRMM observations in terms of shape (power law range

with large-event cutoff). However, quantitative differences exist in the large-event cutoff values. Under global warming (specifically the SSP5-8.5 scenario at the end of the twenty-first century), every model analyzed shows increases in the large-event cutoff values. The fractional change in probability density of the clusters above the cutoff increases approximately exponentially with cluster size and power. This implies a disproportionate change in the incidence of precipitation clusters with large size as well as clusters with large power values. This is true of all models, although the rate of exponential increase is subject to differences, and is governed by the magnitude of change in the cutoff value.

Cluster centroids (precipitation weighted center-of-mass) help identify the dominant spatial pattern of large-event clusters in observations. In the current climate, the Indian and western Pacific oceans tend to host the highest number of precipitation clusters with large power. This pattern is qualitatively reproduced by the CMIP6 multi-model mean. The CMIP6 models are used to project the spatial pattern of increase in the frequency of clusters with large power values. Climatologically precipitating tropical regions tend to see the largest increases. These regions include the Indian subcontinent, the western Pacific Ocean, the central and east Pacific ITCZs, and parts of South America. These regional hotspots are explainable to a great degree by a CC scaling of the current climate cluster distributions.

The CMIP6 models lack the physics to simulate details of intense precipitation events. A few models trade size for precipitation intensity and generate precipitation clusters that do not texturally correspond to observed storm systems (Figure S4 in Supporting Information S1). This issue is particularly egregious for models with much larger  $a_L$  values than observed (Figure S3 in Supporting Information S1), and is likely a consequence of the drizzle problem in climate models (Dai, 2006; Hagos et al., 2021). The model precipitation clusters must therefore be interpreted as being analogous to—but not in one-to-one correspondence with—observed precipitation clusters. Despite these shortcomings, the models are still in agreement that the incidence of heavily precipitating systems is projected to increase under global warming. Future work should confirm these results using higher-resolution models with realistic convective physics. The projected increases in large values of cluster-integrated rainfall could be particularly consequential for vulnerable coastal societies in the Indian subcontinent and western Pacific islands (e.g., Dasgupta et al., 2009; Karim & Mimura, 2008; Nurse et al., 2014.)

## Data Availability Statement

The TRMM 3B42 data used here can be accessed from <https://doi.org/10.5067/TRMM/TMPA/3H/7>. The CMIP6 model data used can be obtained from <https://esgf-node.llnl.gov/projects/esgf-llnl/>. More details about the models can be found in Table S1 in Supporting Information S1.

## Acknowledgments

This study was supported in part by the National Science Foundation grant AGS-1936810.

## References

- Ahmed, F., & Neelin, J. D. (2019). Explaining scales and statistics of tropical precipitation clusters with a stochastic model. *Journal of the Atmospheric Sciences*, 76(10), 3063–3087. <https://doi.org/10.1175/jas-d-18-0368.1>
- Allen, M. R., & Ingram, W. J. (2002). Constraints on future changes in climate and the hydrologic cycle. *Nature*, 419(6903), 228–232. <https://doi.org/10.1038/nature01092>
- Chou, C., & Neelin, J. D. (2004). Mechanisms of global warming impacts on regional tropical precipitation. *Journal of Climate*, 17, 2688–2701. [https://doi.org/10.1175/1520-0442\(2004\)017<2688:mogwio>2.0.co;2](https://doi.org/10.1175/1520-0442(2004)017<2688:mogwio>2.0.co;2)
- Dai, A. (2006). Precipitation characteristics in eighteen coupled climate models. *Journal of Climate*, 19(18), 4605–4630. <https://doi.org/10.1175/jcli3884.1>
- Dasgupta, S., Laplante, B., Murray, S., & Wheeler, D. (2009). *Climate change and the future impacts of storm-surge disasters in developing countries*. (p. 182). Center for Global Development Working Paper.
- Doswell III, C. A., Brooks, H. E., & Maddox, R. A. (1996). Flash flood forecasting: An ingredients-based methodology. *Weather and Forecasting*, 11(4), 560–581. [https://doi.org/10.1175/1520-0434\(1996\)011<0560:fffaib>2.0.co;2](https://doi.org/10.1175/1520-0434(1996)011<0560:fffaib>2.0.co;2)
- Eyring, V., Bony, S., Meehl, G. A., Senior, C. A., Stevens, B., Stouffer, R. J., & Taylor, K. E. (2016). Overview of the coupled model inter-comparison project phase 6 (CMIP6) experimental design and organization. *Geoscientific Model Development*, 9(5), 1937–1958. <https://doi.org/10.5194/gmd-9-1937-2016>
- Fischer, E. M., & Knutti, R. (2015). Anthropogenic contribution to global occurrence of heavy-precipitation and high-temperature extremes. *Nature Climate Change*, 5(6), 560–564. <https://doi.org/10.1038/nclimate2617>
- Hagos, S. M., Leung, L. R., Garuba, O. A., Demott, C., Harrop, B., Lu, J., & Ahn, M.-S. (2021). The relationship between precipitation and precipitable water in CMIP6 simulations and implications for tropical climatology and change. *Journal of Climate*, 34(5), 1587–1600. <https://doi.org/10.1175/JCLI-D-20-0211.1>
- Hamada, A., & Takayabu, Y. N. (2018). Large-scale environmental conditions related to midsummer extreme rainfall events around Japan in the TRMM region. *Journal of Climate*, 31(17), 6933–6945. <https://doi.org/10.1175/jcli-d-17-0632.1>

- Huffman, G. J., Bolvin, D. T., Nelkin, E. J., Wolff, D. B., Adler, R. F., Gu, G., et al. (2007). The TRMM multisatellite precipitation analysis (TMPA): Quasi-global, multiyear, combined-sensor precipitation estimates at fine scales. *Journal of Hydrometeorology*, 8(1), 38–55. <https://doi.org/10.1175/jhm560.1>
- Karim, M. F., & Mimura, N. (2008). Impacts of climate change and sea-level rise on cyclonic storm surge floods in Bangladesh. *Global Environmental Change*, 18(3), 490–500. <https://doi.org/10.1016/j.gloenvcha.2008.05.002>
- Kharin, V. V., Zwiers, F., Zhang, X., & Wehner, M. (2013). Changes in temperature and precipitation extremes in the CMIP5 ensemble. *Climatic Change*, 119(2), 345–357. <https://doi.org/10.1007/s10584-013-0705-8>
- Martinez-Villalobos, C., & Neelin, J. D. (2018). Shifts in precipitation accumulation extremes during the warm season over the United States. *Geophysical Research Letters*, 45(16), 8586–8595.
- Martinez-Villalobos, C., & Neelin, J. D. (2019). Why do precipitation intensities tend to follow gamma distributions? *Journal of the Atmospheric Sciences*, 76(11), 3611–3631. <https://doi.org/10.1175/jas-d-18-0343.1>
- Muller, C., & Takayabu, Y. (2020). Response of precipitation extremes to warming: What have we learned from theory and idealized cloud-resolving simulations, and what remains to be learned? *Environmental Research Letters*, 15(3), 035001. <https://doi.org/10.1088/1748-9326/ab7130>
- Neelin, J. D., Sahany, S., Stechmann, S. N., & Bernstein, D. N. (2017). Global warming precipitation accumulation increases above the current-climate cutoff scale. *Proceedings of the National Academy of Sciences*, 114(6), 1258–1263. <https://doi.org/10.1073/pnas.1615333114>
- Nurse, L. A., McLean, R. F., Agard, J., Briguglio, L. P., Duvat-Magnan, V., Pelesikoti, N., et al. (2014). Cambridge University Press.
- O’Gorman, P. A. (2012). Sensitivity of tropical precipitation extremes to climate change. *Nature Geoscience*, 5(10), 697–700.
- O’Gorman, P. A. (2015). Precipitation extremes under climate change. *Current Climate Change Reports*, 1(2), 49–59.
- O’Gorman, P. A., & Schneider, T. (2009). The physical basis for increases in precipitation extremes in simulations of 21st-century climate change. *Proceedings of the National Academy of Sciences*, 106(35), 14773–14777.
- O’Neill, B. C., Tebaldi, C., Vuuren, D. P., Van, Eyring, V., Friedlingstein, P., Hurtt, G., et al. (2016). The scenario model intercomparison project (ScenarioMIP) for CMIP6. *Geoscientific Model Development*, 9(9), 3461–3482.
- Peduzzi, P., Chatenoux, B., Dao, H., De Bono, A., Herold, C., Kossin, J., et al. (2012). Global trends in tropical cyclone risk. *Nature Climate Change*, 2(4), 289–294. <https://doi.org/10.1038/nclimate1410>
- Peters, O., Christensen, K., & Neelin, J. D. (2012). Rainfall and dragon-kings. *The European Physical Journal – Special Topics*, 205(1), 147–158. <https://doi.org/10.1140/epjst/e2012-01567-5>
- Peters, O., Deluca, A., Corral, A., Neelin, J. D., & Holloway, C. E. (2010). Universality of rain event size distributions. *Journal of Statistical Mechanics: Theory and Experiment*, 2010(11), P11030. <https://doi.org/10.1088/1742-5468/2010/11/p11030>
- Quinn, K. M., & Neelin, J. D. (2017a). Distributions of tropical precipitation cluster power and their changes under global warming. Part I: Observational baseline and comparison to a high-resolution atmospheric model. *Journal of Climate*, 30(20), 8033–8044. <https://doi.org/10.1175/JCLI-D-16-0683.1>
- Quinn, K. M., & Neelin, J. D. (2017b). Distributions of tropical precipitation cluster power and their changes under global warming. Part II: Long-term time dependence in coupled model intercomparison project phase 5 models. *Journal of Climate*, 30(20), 8045–8059. <https://doi.org/10.1175/JCLI-D-16-0701.1>
- Roca, R., & Fiolleau, T. (2020). Extreme precipitation in the tropics is closely associated with long-lived convective systems. *Communications Earth & Environment*, 1(1), 1–6. <https://doi.org/10.1038/s43247-020-00015-4>
- Romps, D. M. (2011). Response of tropical precipitation to global warming. *Journal of the Atmospheric Sciences*, 68(1), 123–138. <https://doi.org/10.1175/2010jas3542.1>
- Stechmann, S. N., & Neelin, J. D. (2014). First-passage-time prototypes for precipitation statistics. *Journal of the Atmospheric Sciences*, 71(9), 3269–3291. <https://doi.org/10.1175/jas-d-13-0268.1>
- Stott, P. A., Stone, D. A., & Allen, M. R. (2004). Human contribution to the European heatwave of 2003. *Nature*, 432(7017), 610–614. <https://doi.org/10.1038/nature03089>
- Tan, J., Jakob, C., Rossow, W. B., & Tselioudis, G. (2015). Increases in tropical rainfall driven by changes in frequency of organized deep convection. *Nature*, 519(7544), 451–454. <https://doi.org/10.1038/nature14339>
- Teo, C.-K., Huynh, H.-N., Koh, T.-Y., Cheung, K., Legras, B., Chew, L., & Norford, L. (2017). The universal scaling characteristics of tropical oceanic rain clusters. *Journal of Geophysical Research: Atmospheres*, 122(11), 5582–5599. <https://doi.org/10.1002/2016jd025921>
- Trenberth, K. E. (2011). Changes in precipitation with climate change. *Climate Research*, 47(1–2), 123–138. <https://doi.org/10.3354/cr00953>

## References From the Supporting Information

- Andrews, M. B., Ridley, J. K., Wood, R. A., Andrews, T., Blockley, E. W., Booth, B., et al. (2020). Historical simulations with HadGEM3-GC3.1 for CMIP6. *Journal of Advances in Modeling Earth Systems*, 12, e2019MS001995. <https://doi.org/10.1029/2019MS001995>
- Boucher, O., Servonnat, J., Albright, A. L., Aumont, O., Balkanski, Y., Bastrikov, V., et al. (2020). Presentation and evaluation of the IPSL-CM6A-LR climate model. *Journal of Advances in Modeling Earth Systems*, 12(7), e2019MS002010.
- Cao, J., Ma, L., Liu, F., Chai, J., Zhao, H., He, Q., et al. (2021). NUIST ESM v3 data submission to CMIP6. *Advances in Atmospheric Sciences*, 38(2), 268–284. <https://doi.org/10.1007/s00376-020-0173-9>
- Tatebe, H., Ogura, T., Nitta, T., Komuro, Y., Oguchi, K., Takemura, T., et al. (2019). Description and basic evaluation of simulated mean state, internal variability, and climate sensitivity in MIROC6. *Geoscientific Model Development*, 12(7), 2727–2765. <https://doi.org/10.5194/gmd-12-2727-2019>
- Voltaire, A., Saint-Martin, D., S n si, S., Decharme, B., Alias, A., Chevallier, M., et al. (2019). Evaluation of CMIP6 deck experiments with CNRM-CM6-1. *Journal of Advances in Modeling Earth Systems*, 11(7), 2177–2213. <https://doi.org/10.1029/2019ms001683>
- Wu, T., Lu, Y., Fang, Y., Xin, X., Li, L., Li, W., et al. (2019). The Beijing Climate Center climate system model (BCC-CSM): The main progress from CMIP5 to CMIP6. *Geoscientific Model Development*, 12(4), 1573–1600. <https://doi.org/10.5194/gmd-12-1573-2019>
- Yukimoto, S., Kawai, H., Koshiro, T., Oshima, N., Yoshida, K., & Urakawa, S. (2019). The meteorological research institute earth system model version 2.0, MRI-ESM2.0: Description and basic evaluation of the physical component. *Journal of the Meteorological Society of Japan. Series II*. <https://doi.org/10.2151/jmsj.2019-051>
- Ziehn, T., Chamberlain, M. A., Law, R. M., Lenton, A., Bodman, R. W., Dix, M., & Srbinsky, J. (2020). The Australian earth system model: ACCESS-ESM1. 5. *Journal of Southern Hemisphere Earth Systems Science*, 70(1), 193–214. <https://doi.org/10.1071/es19035>